Deformation Twinning in Zirconium:
Direct Experimental Observations and Polycrystal Plasticity Predictions

Jaiveer Singh[1], S. Mahesh[2], Gulshan Kumar[1], Prita Pant[1], D. Srivastava[3], G. K. Dey[3], N. Saibaba[4] and I. Samajdar[1]

[1]Department of Metallurgical Engineering & Materials Science, Indian Institute of Technology Bombay, Powai, Mumbai-400 076, India

[2]Department of Aerospace Engineering, Indian Institute of Technology Madras, Chennai-600 036, India

[3]Materials Science Division, Bhabha Atomic Research Centre, Trombay, Mumbai-400 085, India

[4]Nuclear Fuel Complex, Hyderabad-500 062, India

Abstract

Deformation twinning was directly observed in three commercial zirconium alloy samples during split channel die plane-strain compression. One pair of samples had similar starting texture but different grain size distributions, while another pair had similar grain size distribution but different starting textures. Extension twinning was found to be more sensitive to the starting texture than to the grain size distribution. Also, regions of intense deformation near grain boundaries were observed. A hierarchical binary-tree based polycrystal plasticity model, implementing the Chin-Hosford-Mendorf twinning criterion, captured the experimentally observed twinning grains' lattice orientation distribution and the twin volume fraction evolution, provided the critical resolved shear stress for extension twinning, τ_0, was assumed much larger than any of the values reported in the literature, based on the viscoplastic self-consistent model. A comparison of the models suggests that τ_0 obtained using the present model and the viscoplastic self-consistent models physically correspond to the critical stress required for twin nucleation, and twin growth, respectively.

Keywords: zirconium, deformation twinning, plastic deformation, plane strain compression, EBSD, polycrystal plasticity.

I. INTRODUCTION

The deformation behavior of hexagonal closed packed (hcp) metals is more complex than that of cubic metals [1]. Plastic deformation in hcp zirconium alloys is accommodated by the activation of slip systems [2–6] together with deformation twinning systems [7–11]. The set of potentially activated slip and twinning systems is temperature dependent. Deformation twinning can have a significant effect on microstructural development and mechanical behavior [10,12–17]. This has important consequences in the context of zirconium alloy components, whose fabrication and in-reactor usage are associated with inelastic deformation [18,19].

Material purity, microstructure, texture, processing temperature, strain mode, and strain-rate are well-established parameters that influence deformation twinning in pure zirconium and zirconium alloys. Akhtar and Teghtsoonian [20] showed that alloying elements influence the shape of the hardening curve of single crystals. Reduced grain size has been shown to inhibit deformation twinning [21–23], and grain boundary character has been shown to be important in determining the ease of twin nucleation [24]. Crystallographic texture influences the resolved shear stresses on slip and twinning systems, and thus influences the extent of deformation twinning significantly [3,5,20,21,23,25–29]. The critical resolved shear stress of deformation twinning systems increases less rapidly with decreasing temperature than that of slip systems. Consequently, more deformation twinning occurs at lower temperatures [5,30].

Much research spanning several decades has gone into incorporating deformation twinning into polycrystal plasticity models [17,31–33]. Highlights include the pioneering model due to Chin et al. [31], proposed for face centered cubic materials. In this model, each twinning system is associated with a critical resolved shear stress and twin growth is governed by Schmid's law [34]. Twinning is thus treated on par with unidirectional slip by assigning critical resolved shear stresses with or without hardening to twinning systems. The methodology to implement the Chin et al. model in rate-independent polycrystals, given by van Houtte [32], was another important step. Understanding the transition from 'copper'-type to 'brass'-type textures in face centered cubic metals [32], wherein the interplay between twinning and slip system hardening was found crucial [35], represented an important achievement of these models. More recently, it has been firmly established that deformation twinning involves separate nucleation and

propagation stages, either of which may be rate limiting. Recent works on titanium alloys [36–38] and zirconium alloys [39] establish a strong correlation of twin nucleation at a grain boundary with slip transfer across it. The Chin-Hosford-Mendorf model does not account for these microstructural influences on deformation twin nucleation.

Split channel die plane-strain compression (SCDPSC) is an established [40–45] methodology for direct observations on deformed microstructures. This was used in the present study as well. A combination of SCDPSC and electron backscattered diffraction (EBSD) was employed to extract information of twinning parents/products at various stages of plane-strain compression in three samples. One pair of samples had similar initial crystallographic texture but different grain size distributions, while another pair had the same grain size distribution but different starting textures. This study also employed a recently developed [42] EBSD based DIC (digital image correlation): a proven means for extracting information on near boundary mesoscopic shear (NBMS) strains. Visual identification and separation of twins and twinned regions were utilized to address the orientation dependence of deformation twinning in zirconium alloys. The experimental approach is detailed in Sec. II A.

Rate-independent polycrystal plasticity simulations were performed and compared with the experimental data. A number of models to describe the macroscopic plasticity in terms of plastic deformation of individual grains have been proposed [34]. Of these, the classical Taylor [46] model imposes an unphysical strong constraint on individual grains, especially in low symmetry materials. The viscoplastic self-consistent model, proposed by Lebensohn and Tomé [47], models the partitioning of the imposed deformation between hard and soft grains efficiently. However, in the self-consistent model too, mechanical interaction between two grains across a grain boundary facet is not accounted for directly. A more recent binary tree based polycrystal plasticity model [48], which accounts explicitly, albeit approximately for inter-granular interactions has been used in the present work. Following numerous works in the literature [3,6,9,17,24,33,48,49], the Chin, Hosford and Mendorf [31] twinning model is used presently. The modeling aspects have been detailed in Sec. II B.

The experimental results and predictions from simulations are compared, as described in Sec. III. Good agreement is obtained, provided one twinning hardening parameter is taken to be

much larger than any of its values quoted in the literature. This observation is explained in Sec. IV, and the discord is attributed to the modeling treatment of intergranular interactions.

II. EXPERIMENTAL AND SIMULATION DETAILS

A. Experimental Methods

Three samples of a commercial zirconium alloy, Zircaloy-4 whose chemical composition is given in Table I, were studied. These samples were termed generically as samples A1, A2 and B1. A1 and A2 were obtained from hot extruded, albeit fully recrystallized, Zircaloy-4. Specimen B1 was prepared by subjecting A1 to an additional grain coarsening annealing step (760°C/4Hr). As discussed later in Sec. III A, A1 and B1 had differences in average grain size and grain size distribution. Thus, one pair of samples (A1 and A2) had the same starting texture but different grain size distributions, while another pair of samples (A1 and B1) had the same grain size distribution but different starting textures. These were subjected to split channel die plane-strain compression (SCDPSC).

SCDPSC samples were prepared by precision machining two separate specimens. Together they need to fit into the channel die. More details are given Refs. [40–42,50], and latter in section III A and Figure 2 (a). The specimens were wrapped with Teflon™ tape, to reduce frictional effects. Microstructures of the same regions were measured, with progressive strains, through electron-backscattered diffraction (EBSD). Typically, a strain increment of ~0.04 was used. However, the final strain differed between the specimens (ranging from a minimum of 0.12 to a maximum of 0.3). Controlled plastic deformations were provided in a servo-hydraulic testing system (Zwick-Roell™). A grid of micro-indents of the specimen surfaces allowed strain measurements with progressive deformation. It needs to be noted, that appropriate specimen surfaces were subjected to standard metallography and electro-polishing [12]. For the latter, a Struers™ Tenupol-5 system was used with 20:80 perchloric acid: methanol by volume, -20°C and 20 volts dc.

The EBSD measurements were made on a FEI™ Quanta 3D-FEG (field emission gun) SEM (scanning electron microscopy), using TSL-OIM™ EBSD software. The scans were made at identical step size (0.25 μm) and beam/video conditions. For the EBSD analysis, data with

B. Polycrystal plasticity modeling

1. Binary tree-based polycrystal plasticity model

Texture predictions were obtained from polycrystal plasticity simulations performed using the binary-tree based model [48]. In this model, grains are treated as homogeneously deforming rigid-plastic rate-independent domains. Further, aggregates of grains are represented as nodes of a binary tree, a standard data structure [52]. The lowest nodes of the binary tree represent grains. Higher binary tree nodes represent increasingly larger sub-aggregates of grains, culminating with the root of the tree (top most node). The root represents the entire polycrystalline aggregate. Following standard terminology [52], the two nodes $[l(k)]$ and $[r(k)]$ that are 'descended' from a certain 'parent' node $[k]$ in the binary tree are called its 'children'. The children $[l(k)]$ and $[r(k)]$ are then said to be 'siblings' of each other. The volume of the sub-aggregate represented by node $[k]$ will be denoted $w_{[k]}$ in the sequel. It follows that

$$w_{[k]} = w_{[l(k)]} + w_{[r(k)]}. \tag{1}$$

The binary tree representation of the microstructure is exemplified schematically in Figure 1. The simplified microstructure is shown in Figure 1 (a) and the corresponding binary tree is shown in Figure 1 (b). In this simple example, the $4-$faceted central grain interacts with its neighbors across four planar grain boundaries. These interactions are modeled by sub-dividing the original grain into four regions, A, B, C, and D, as shown. Let the sub-divisions of the neighboring grains abutting these four regions be A1, B1, C1 and D1, respectively. The lowest level of the binary tree, shown in Figure 1 (b), represents these interactions across grain boundary facets. Longer range interactions, e.g., that between regions A and B1 are also accounted for in the binary tree based model, through the continuity conditions enforced between the sub-aggregate formed by regions A and A1 (termed 1 in Figure 1 (b)) and that between the sub-aggregates formed by regions B and B1 (termed 2). Still longer-range interactions are also captured, albeit approximately, at higher levels of the binary tree.

The methodology adopted to construct the binary-tree based model of the present microstructure was the following. The EBSD images of the two mirror-polished faces of the split channel die specimen prior to deformation were converted into a list of grains. A grain in the EBSD micrograph was identified by a continuous grain boundary with lattice misorientation threshold of 5°. The conversion process also captured the inter-granular connectivity, i.e., the list of grains neighboring a particular grain 'g'. Grains for which the neighbors were not fully known were omitted. Such grains were typically located near the edges of the micrograph. Each computer grain was divided into as many parts as the number of its neighbors, as shown schematically in Figure 1 (a). The volume fraction of each of these parts with respect to the grain volume was taken to be the same as the length fraction of the grain boundary facet between grain 'g' and its neighbor in the micrograph. Pairs of such grain sub-divisions, taken from across each grain boundary facet form an ALAMEL unit as defined by Van Houtte et al. [53], e.g., pairs (A, A1), (B, B1), (C,C1) and (D,D1) in Figure 1(a) are ALAMEL units. Each ALAMEL unit is comprised of two ALAMEL regions, each of which has a distinct lattice orientation.

A set of 1024 ALAMEL units was extracted by random uniform sampling of all ALAMEL units in the micrographs after weighting each pair by its area fraction in the plane of EBSD observation. The 2048 ALAMEL regions that constitute these ALAMEL units formed the lowest level of a balanced binary-tree based representation of the polycrystal [48]. The EBSD micrograph only gave the traces of grain boundary facets in the plane of observation; their true spatial orientation was not known. Accordingly, the model grain boundary facet within each model ALAMEL unit was assigned a random orientation drawn from the space of all orientations, which yielded the observed trace in the EBSD observation plane. All orientation assignments were performed with respect to the orthogonal reference frame defined by the principal directions of channel die compression: rolling, transverse and normal directions. The interfaces between higher sub-aggregates in the binary tree were assigned orientations drawn from a uniform random distribution of unit vectors. It was verified that the *statistics* of texture evolution or twinning was negligibly sensitive to the choice of these random interface orientations.

In the binary-tree based model [48], field variables such as stresses $\sigma_{[k]}$ and strain-rates $\dot{\varepsilon}_{[k]}$ of node $[k]$ are defined as volume-fraction weighted averages of the corresponding fields over the children:

$$\sigma_{[k]} = \frac{\left\{w_{[l(k)]}\sigma_{[l(k)]} + w_{[r(k)]}\sigma_{[r(k)]}\right\}}{w_{[k]}},$$ (2)

and

$$\dot{\varepsilon}_{[k]} = \frac{\left\{w_{[l(k)]}\dot{\varepsilon}_{[l(k)]} + w_{[r(k)]}\dot{\varepsilon}_{[r(k)]}\right\}}{w_{[k]}}.$$ (3)

The lowest nodes of the binary tree are those with no child nodes, called leaves. They represent grains that obey the rigid-plastic rate-independent constitutive law [34]. Denoting the root of the tree by $[r]$, and the set of all leaf nodes that represent grains in the tree by G, it follows from Eqs. (2) and (3) that

$$\sigma_{[r]} = \sum_{[g]\in G} \sigma_{[g]},$$ (4)

and

$$\dot{\varepsilon}_{[r]} = \sum_{[g]\in G} \dot{\varepsilon}_{[g]}.$$ (5)

In the binary-tree based model, the interface between the sub-aggregates represented by sibling nodes in the binary tree was assumed to be planar. Let the planar interface between the sibling nodes $[l(k)]$ and $[r(k)]$ be oriented normal to $\nu_{[k]}$. Continuity of traction and velocity were imposed between sibling nodes across this planar interface. Thus,

$$\left\{\sigma_{[l(k)]} - \sigma_{[r(k)]}\right\} \cdot \nu_{[k]} = 0,$$ (6)

and

$$t_{[k]} \cdot \left\{\dot{\varepsilon}_{[l(k)]} - \dot{\varepsilon}_{[r(k)]}\right\} \cdot t_{[k]} = 0, \forall\, t_{[k]} \perp \nu_{[k]}.$$ (7)

Lattice rotations of grains and larger sub-aggregates in the binary tree based model were determined by compatibility with their sibling nodes. A detailed discussion of lattice rotations is given in Ref. [48].

2. Grain plasticity

The model hexagonal close packed (hcp) grains are assumed to have the following plastic deformation modes: prismatic slip $(10\bar{1}0) < 11\bar{2}0 >$, pyramidal slip $\{10\bar{1}1\} < 11\bar{2}3 >$, and extension twinning $\{10\bar{1}2\} < 10\bar{1}1 >$ following e.g., Tenchoff [19] and Tomé et al. [54]. Schmid's law [34] governs the activation of all slip and twinning systems. If the critical resolved shear stress of slip system or twinning system s in ALAMEL region g is denoted $\tau_{[g]}^s$, the Schmid tensor of slip system or twinning system s, as $m_{[g]}^s$, then the resolved shear stress on this system is given by $\sigma_{[g]}: m_{[g]}^s$, and

$$\dot{\gamma}_{[g]}^s \begin{cases} = 0, & \text{if } \sigma_{[g]}: m_{[g]}^s < \tau_{[g]}^s \\ \geq 0, & \text{if } \sigma_{[g]}: m_{[g]}^s = \tau_{[g]}^s \\ \text{undefined, otherwise.} \end{cases} \tag{8}$$

In this scheme, the two senses of slip (positive and negative Burgers vectors) of a slip system are regarded as two different slip systems. Twinning systems have only sense of shear.

Slip and twinning systems are assumed to harden following the extended Voce law [54,55]. Suppressing the subscript g for clarity,

$$\hat{\tau}^s = \hat{\tau}_0^s + (\tau_1^s + \theta_1^s \Gamma) \left\{ 1 - \exp\left(-\frac{\theta_0^s \Gamma}{\tau_1^s} \right) \right\}, \tag{9}$$

where, τ_0^s, τ_1^s, θ_0^s, and θ_1^s denote material constants associated with slip system s and Γ denotes the total accumulated slip in the grain. Interaction between the various slip and twinning modes was captured using the self (h_{ss}) and latent ($h_{ss'}$) hardening coefficients [55]:

$$\dot{\tau}^s = \frac{d\hat{\tau}^s}{d\Gamma} \sum_{s'} h_{ss'} \dot{\gamma}^s, \tag{10}$$

where τ_s denotes the critical resolved shear stress (CRSS) of slip system s, $\dot{\tau}_s$ denotes the rate of change of the CRSS of slip system s, and $\dot{\gamma}^s$ denotes the slip rate in system s.

Activation of twinning systems and accommodation of shear by their activation entails a transformation of the lattice orientation of the grain matrix [10,34]. Following the methodology

proposed by Van Houtte [32], the volume fraction f_t of twin variant t depends on the accumulated shear γ_t in twinning system t and its characteristic twinning shear, Γ_t as:

$$f_t = \gamma_t / \Gamma_t. \tag{11}$$

In zirconium alloys [10,34], $\Gamma_t = 0.169$ for the six variants of $\{10\bar{1}2\} < 10\bar{1}1 >$ extension twins. The growth of twins is accounted for simply by the increase of f_t in the model. Twinned volumes are not explicitly expressed as new leaf nodes in the binary tree based model. Thus, slip or re-twinning within the twinned volume is not modeled. However, if the volume fraction of twin variant t exceeds a pre-set threshold of $f_0 = 0.8$, i.e., if $f_t \geq f_0 = 0.8$, the lattice orientation of the parent grain is completely reoriented to that of twin variant t.

3. Comparison with the viscoplastic self-consistent model

While the present binary tree based model shares certain commonalities with the classical viscoplastic self-consistent model due to Lebensohn and Tomé [47], which has been extensively applied in twinning studies, there are also key differences. The commonalities are the assumption of homogeneous deformation of the grains or ALAMEL regions, the use of a critical resolved shear stress for twinning, and the non-accounting for explicit twin nucleation. Equations (6) and (7) represent the most significant departure of the binary-tree based model from the viscoplastic self-consistent model of Lebensohn and Tomé [47].

In the viscoplastic self-consistent model [47,54], grains do not directly interact with their neighbors. A typical grain g deforms compatibly with a homogeneous effective medium representing the entire polycrystal through an interaction equation of the form

$$\dot{\varepsilon}_{[g]} - < \dot{\varepsilon}_{[g]} > = M\left(\sigma_{[g]} - < \sigma_{[g]} >\right). \tag{12}$$

In Eq. (12), angle brackets denote averaging over all grains. These average strain-rate and stress fields correspond to the homogeneous effective medium. M, the localization tensor, controls the deviation of grain fields from the macroscopic fields, and itself depends on the polycrystalline deformation gradient and an appropriately scaled plastic modulus of the polycrystal. Tome et al. [54] selected the scaling so as to obtain the activation of expected slip systems in grains.

The constraint on a grain expressed by Eq. (12) thus, does not explicitly account for the granular neighborhood of g. Nevertheless, writing out Eq. (12) for *any* pair of grains g_1 and g_2, and subtracting them from each other yields

$$\dot{\varepsilon}_{[g_1]} - \dot{\varepsilon}_{[g_2]} = M(\sigma_{[g_1]} - \sigma_{[g_2]}). \tag{13}$$

In the binary tree based model described in Sec. II B, each ALAMEL region g_1, which represents part of grain, must deform compatibly with its neighboring ALAMEL region, say g_2 across a grain boundary facet following Eqs. (6) and (7). Consider a coordinate system whose x_3 axis is aligned normal to the grain boundary facet. Then, Eqs. (6) and (7) amount to

$$\begin{aligned} \dot{\varepsilon}_{[g_1],11} &= \dot{\varepsilon}_{[g_2],11} \\ \dot{\varepsilon}_{[g_1],22} &= \dot{\varepsilon}_{[g_2],22} \text{ , and} \\ \dot{\varepsilon}_{[g_1],12} &= \dot{\varepsilon}_{[g_2],12} \end{aligned} \tag{14}$$

$$\begin{aligned} \sigma_{[g_1],33} &= \sigma_{[g_2],33} \\ \sigma_{[g_1],13} &= \sigma_{[g_2],13} \text{ .} \\ \sigma_{[g_1],23} &= \sigma_{[g_2],23} \end{aligned} \tag{15}$$

Let $\dot{\varepsilon}_{[g_1]} = \{\dot{\varepsilon}_{[g_1],11} \quad \dot{\varepsilon}_{[g_1],22} \quad \dot{\varepsilon}_{[g_1],33} \quad \dot{\varepsilon}_{[g_1],12} \quad \dot{\varepsilon}_{[g_1],23} \quad \dot{\varepsilon}_{[g_1],13}\}^T$, and let $\sigma_{[g_1]} = \{\sigma_{[g_1],22} \quad \sigma_{[g_1],22} \quad \sigma_{[g_1],33} \quad \sigma_{[g_1],12} \quad \sigma_{[g_1],23} \quad \sigma_{[g_1],13}\}^T$. $\dot{\varepsilon}_{[g_2]}$ and $\sigma_{[g_2]}$ can be expressed likewise. Then Eqs. (14) and (15) can be recast in the form

$$\dot{\varepsilon}_{[g_1]} - \dot{\varepsilon}_{[g_2]} = N(\sigma_{[g_1]} - \sigma_{[g_2]}), \tag{16}$$

where,

$$N = \begin{pmatrix} 0 & 0 & 0 & 0 & 0 & 0 \\ 0 & 0 & 0 & 0 & 0 & 0 \\ 0 & 0 & \infty & 0 & 0 & 0 \\ 0 & 0 & 0 & 0 & 0 & 0 \\ 0 & 0 & 0 & 0 & \infty & 0 \\ 0 & 0 & 0 & 0 & 0 & \infty \end{pmatrix}. \tag{17}$$

Comparing Eq. (13) from the viscoplastic self-consistent model and Eq. (16) from the binary tree based model, it is clear that grains in the two models are constrained entirely differently. However, because of the zero and infinite values on the diagonal of the matrix N, the constraints

exerted upon grains by the two models are not directly comparable, i.e., 1it is not possible to characterize one model or the other as producing the stronger constraint upon grains.

Other differences between the viscoplastic self-consistent model [47] and the present binary tree based model are: (i) while the former model assumes rate-dependence, both rate-dependent [48] and rate-independent versions of the latter are available. The present work utilizes the rate-independent version due to its mathematically guaranteed numerical convergence regardless of the distorted shape of the single crystal yield surface. (ii) The mechanics of texture evolution in the two models is different. In the latter model, the rate of lattice rotation is determined by compatibility with neighbors, but not in the former model.

It is also important to note that not all intergranular interactions are directly considered in the binary tree based model. In this respect, the binary tree based model differs from the crystal plasticity finite element method. Consider for e.g., the idealized four-grain microstructure of Figure 1 (a). Here, even though ALAMEL region pairs (A, B), (B, C), (C, A), and (C, D) abut each other, they interact only indirectly in the binary-tree based model. For instance, the continuity conditions between pair (A, B) is subsumed within the interaction of ALAMEL unit (A, A1) with (B, B1). This reduction in the number of modeled interactions is the reason for the superior computational performance of the binary-tree based model, comparable to that of the classical Taylor model [48].

4. Material point deformation

Let $v_i(x_k)$ denote the material flow velocity at spatial coordinate x_k. Let

$$L_{ij}(x_k) = \frac{\partial v_i}{\partial x_k}; i,j \in \{RD, TD, ND\} \tag{18}$$

denote the velocity gradient at spatial coordinate x_k. In channel die compression with perfectly lubricated contacts between the die and billet,

$$[L]_{RD-TD-ND} = \begin{bmatrix} 1 & L_{RD,TD} & L_{RD,ND} \\ 0 & 0 & 0 \\ 0 & 0 & -1 \end{bmatrix}, \tag{19}$$

following the relaxed constraints model of Honeff and Mecking [56]. The two components $L_{RD,TD}$ and $L_{RD,ND}$ were left unspecified. Instead,

$$\sigma_{[r]_{RD,TD}} = \sigma_{[r]_{RD,ND}} = 0 \tag{20}$$

was imposed.

III.   RESULTS

A. Experimental

Figure 2 (a) shows a schematic diagram of the split channel die plane-strain compression (SCDPSC) set-up. SCDPSC was popularized by Chin et al. [57] as early as 1966. It permits the imposition of a near-ideal plane strain compression deformation path. A great advantage of this technique is that it allows direct observation of split samples [40]. Chapelle and Darrieulat [45] deposited micro grids on sample surface. This allowed local strain quantification of the deformation steps at various scales. Also, the force-displacement data during SCDPSC can be easily converted to stress-strain behavior. Small strain steps may be taken during loading. This allows for better understanding of microstructure evolution.

Three samples were used: A1, A2 and B1. As also indicated in Figure 2 (a), A2 was obtained by rotating A1 90° about TD. Figure 2 (b) shows the $\varphi_2 = 30°$ ODF section of starting textures for the samples. The figures also indicate the maximum ODF intensities ($f(g)_{max}$) and texture indices, defined as:

$$\text{Texture Index (TI)} = \int (f(g)^2)dg. \tag{21}$$

Texture indices are considered a more effective representation of relative anisotropy than the conventional $f(g)_{max}$ values [58]. As shown in Figure 2 (b), A1 had a rotated basal (0001) texture. A2 and B1 had similar, but not identical, textures with dominant $< uvtw >$ fibers of $< \bar{1}100 >$ and $< 1\bar{1}00 >$. The samples also had differences in grain sizes and in grain size distributions, see Figure 2 (c). For example, A1 and A2 had finer (11 μm) average grain size than B1 (18 μm). A1 and A2 also had a clear bimodal distributions in grain size whereas B1 shows a unimodal grain size distributions. Figure 2 (d) collates EBSD observations from the SCDPSC

specimens of A1 and B1. Though results presented in Figure 2 (d) were obtained from one side of the split SCDPSC specimens, the other side was used for statistics and confirmation of reproducibility. The direct observations, as in Figure 2 (d), captured formation and growth of deformation twinning.

The Taylor factor distributions, estimated for prismatic slip, were similar for all the specimens, as shown in Figure 3 (a). However, the work hardening behaviors were significantly different. This is shown in Figure 3 (b) as $\frac{d\sigma}{d\varepsilon}$ versus σ plots, where σ and ε represent true stress and true strain along the normal direction, respectively. The work hardening in A1 was clearly more pronounced than in A2 and B1. The estimated length fraction of visible twin boundaries (length of 'new' twin boundaries normalized by the length of all the high angle boundaries) and the area fractions of twinned regions are shown in Figure 4 (a) and 4 (b), respectively. The figures clearly show significantly more twinning in sample A1. Comparable twinning was observed in samples A2 and B1. Whereas samples A1 and A2 had similar grain size distributions, samples A2 and B1 had comparable starting texture. Figure 4 suggests that twinning is more influenced by starting texture than by grain size distribution.

Signatures of misorientation developments were obtained as kernel average misorientation or KAM (Figure 5 (a)), grain average misorientation or GAM (Figure 5 (b)) and grain average misorientation spread or GOS (Figure 5 (c)). KAM represents the average misorientation between each measurement point and its immediate neighbors: provided such misorientation does not exceed a critical value. The latter was taken as 5° in this study. For estimations of GAM and GOS, a grain definition is critical. A grain was defined by the presence of a continuous boundary of ≥ 5° misorientation. GAM represents average point-to-point misorientation inside such a grain. GOS, on the other hand, represents misorientation between all measurement points of a grain and the grain average (quaternion average) orientation. A2 had the highest misorientation (for all three indices of KAM, GAM and GOS) followed by A1, while B1 was with the lowest values. In other words, quantitative data on direct misorientation developments clearly showed that: (i) the bimodal grain size distribution enabled more misorientation development (comparison between A2 and B1) and (ii) so did less twinning (comparison between A2 and A1). (ii) is not unexpected. Past study [21] also showed that suppression of twinning and more crystallographic slip leads to stronger misorientation

developments. The observations in Figure 5 (d) and 5 (e) are, however, new. They clearly show that the twin-parent grains had more misorientation (and misorientation developments) than the non-twinned grains. Both were taken at 10% sample height reduction. This prompts the question: whether prior-twinning misorientation developments played a role in twin nucleation.

To explore this point further, local strain measurements were performed. An earlier study [42] had used EBSD-based DIC (digital image correlation). This enabled extraction of near boundary mesoscopic shear (NBMS) in SCDPSC Zircaloy-4. This was repeated presently for different grains in samples A1 and B1. Figure 6 (a) provides local shear strain developments in a cluster of grains at 4% specimen height reduction. NBMS was present at both sides of a grain boundary, and appeared to balance/compensate each other. As shown in Figure 6 (b), sample A1 had more NBMS at 10% reduction. The same conclusion was found valid for other strains as well. The NBMS can be represented as [42] maximum shear strain, grain average shear strain and local shear strains. The first two are in number fractions of the associated pixels, while local shear was represented in terms of area fractions. As collated in Figure 6 (c), all representations of NBMS were higher, in both samples, for the so-called twin-parent grains. In other words, it was shown that grains with visible twinning were also associated with significantly higher near boundary mesoscopic shear strains.

B. Twinning predictions

It is generally impractical to accurately predict the specific set of twinning grains from a microstructure. This is because the deterministic mechanical stress and strain-rate fields predicted by any polycrystal plasticity model widely diverge from experimental observations. This is true for even the most spatially resolved crystal plasticity finite element method [59,60]. This divergence is partly because the mechanical field predictions, which are made on the basis of a model constructed from a two dimensional microstructure, are sensitive to the grain shapes and interactions in the third dimension [61]. At best, therefore, one may expect to glean only statistically accurate predictions from simulations. Therefore, in the present study it was only attempted to predict the *statistical distribution* of twinning grains in orientation space.

The experimentally measured area fraction evolution of extension twins in the three specimens A1, A2 and B1 is shown in Figure 7. A reasonable match of the experimental

twinning evolution with the predictions from the binary-tree based model was obtained using the extended Voce hardening parameters listed in Table II. These hardening parameters were identical to those of Tomé et al. [54], excepting τ_0 of the $\{10\bar{1}2\} < \bar{1}011 >$ extension twinning systems. It was found necessary to effect a five-fold increase in the value of τ_0 over the value given by Tomé et al. [54], in order to obtain the fit in Figure 7. It is noteworthy that employing the hardening parameters listed in Table II, a relaxed constraints (Eq. (19)) Taylor model predicts a much smaller twin volume fraction evolution in specimen A1, and no twinning at all in specimens A2 and B1.

To explore the orientation of grains undergoing deformation twinning, focus was concentrated on the strain level corresponding to 4% reduction. The distribution of twinning and non-twinning grains in orientation space is depicted in an Euler space map in the $\varphi_1 - \varphi$ plane in Figure 8. This representation disregards the Euler angle φ_2 and the volume fraction of grains. Instead, each dot in this map corresponds to one grain located at the coordinates (φ_1, φ) of that grain. Special points in the $\varphi_1 - \varphi$ plane that correspond to alignments of the c −axis with any of the macroscopic loading directions are marked in Figure 8 (a).

Figure 8 (b) shows the set of all grains in the EBSD specimen, together with those observed experimentally to have twinned and those observed experimentally not to have twinned at 4% reduction, in an Euler space map in the $\varphi_1 - \varphi$ plane. The initial orientation of the grains predicted to twin is shown in Figure 8 (c). The predictions are seen to qualitatively agree with experiment (Figure 8 (b)). In specimen A1, twinning is predicted along the $\varphi_1 = 90°$ line, which corresponds to orientations for which the grain c −axes were aligned close to the RD-TD plane. In specimens A2 and B1, twinning was predicted for orientations wherein the c −axis alignment lay between $c \parallel$ TD, and $c \parallel$ (TD+ND)/$\sqrt{2}$. In the experimental Figure 8 (b), however, it was seen that only grains near $c \parallel$ TD twin. The predictions thus overestimated the set of twinning orientations in these two specimens also. In all three specimen, the region of orientation space over which twinning is predicted is larger than that over which twins are experimentally observed. These observations, based on the Euler space maps, are corroborated by the ODF sections at $\varphi_2 = 30°$, shown in Figure 9 (a) and (b).

As noted above, the relaxed constraints Taylor model with hardening parameter τ_0 of the $\{10\bar{1}2\} < \bar{1}011 >$ extension twinning system predicts no twinning in specimens A2 and B1. Figure 8 (d) plots the orientations predicted to twin assuming the reduced value $\tau_0 = 70$ MPa for the $\{10\bar{1}2\} < \bar{1}011 >$ extension twinning system (equal to that of the prismatic slip systems). According to the Taylor model, the twinning grain orientations are clustered around orientations with $c \parallel$ (TD+ND)/$\sqrt{2}$ in specimen A2 and B1. This strongly disagrees with experimental observations. Regions of orientation space found to twin experimentally and in the simulations are nearly disjoint. These observations are also reflected in the ODF sections at $\varphi_2 = 30°$, shown in Figure 9 (c).

The predictions of the relaxed constraints Taylor model diverge from experimental observations. This is because the Taylor model, when applied to low symmetry materials, imposes a physically unrealistic deformation constraint on grains [34]. The binary tree model, on the other hand, appears to model the constraint imposed upon grains by the polycrystal better. This leads to better qualitative comparison between the binary tree model predictions and the experiment.

Histograms showing the total slip and twinning shear accumulated in twinning and non-twinning grains, as predicted by the simulations in specimen A1 at 4% channel die compression are shown in Figure 10. The mean accumulated shear in the twinning grains, is about 1.7 times greater than that in the non-twinning grains. The predicted histograms are not quantitatively comparable with those obtained experimentally, shown in Figure 6. However, qualitatively, the simulations predict, in accord with experiments, that twinning grains deform more than non-twinning grains in the polycrystal.

IV. DISCUSSION

In this manuscript, three polycrystalline zirconium alloy specimens were subjected to split channel die plane strain compression. Near grain boundary shear strains were estimated through a newly developed [42] EBSD-DIC technique. The objective of this exercise was to explore the possible role of near boundary shear in deformation twinning. Measurements clearly showed higher shear for grains subsequently undergoing deformation twinning (Figure 6 (c)). This translated into more shear in specimen A1 than in B1 (Figure 6 (b)). As more near boundary

shear strain corresponds to higher misorientation development in zirconium [42], it is hence expected that specimen A1 (with the maximum twinning) also had the most extensive in-grain misorientation developments (see Figure 5). These observations indicate that near grain boundary shear formed prior to twinning and corresponding misorientation developments played a role in the nucleation of deformation twins.

It has long been hypothesized [62,63] that hard deformation modes activate near the grain boundaries in low symmetry hexagonal materials. This inhomogeneous activation is enabled by high near boundary stress concentrations. Some of the observed near boundary modes in zirconium alloys at room temperature are $\{11\bar{2}3\}$ slip [64] and basal slip [65]. Nucleation of $\{10\bar{1}2\}$ extension twins at grain boundaries may represent another accommodation mechanism in zirconium at room temperature [62,66]. While hard slip modes activated near grain boundaries remain confined to that region, twins nucleated near grain boundaries propagate into the grain bulk under a favorable state of shear stress.

The binary tree based model captured the twinning rate and twinning orientations observed experimentally. The favorable comparisons between experiment and binary tree based model were obtained assuming the following slip and twinning deformation modes: prismatic slip, $< c + a >$ pyramidal slip, and extension twinning. Extension twinning systems are assumed to activate following the classical Chin-Hosford-Mendorf model. The same extended Voce hardening parameters, as assumed by Tomé et al. [54], sufficed for the prismatic and $< c + a >$ pyramidal slip systems. However, it was found essential to increase the critical resolved shear stress (CRSS) of the extension twinning system by a factor of five (from 50 MPa in Tomé et al. [54] to 250 MPa presently), in order to capture the twin volume fraction evolution. Values of τ_0 any lower than 250 MPa result in more profuse twinning than that experimentally observed.

Tomé et al. [54] assumed a ratio of 10 between the hardness of extension twinning systems to the initial hardness of prismatic slip systems. Other researchers have reported smaller ratios in zirconium alloys at room temperature. Lebensohn et al. [67] and Girard et al. [68] assumed a ratio of 1.5 to explain the texture of pilgered zirconium alloy. Kaschner et al. [6] reported a ratio of about 5. Gloaguen et al. [69], used a hardness ratio of extension twinning to prismatic slip of 2 in conjunction with an elastoplastic self-consistent model. In the study of

Capolungo et al. [70], twin nucleation and twin propagation were treated separately with the critical resolved shear stress needed for the former being much higher. Even so, the ratio of the critical twin nucleation shear stress is about 4 times larger than their initial prismatic slip system hardness. It is clear that the initial hardness ratio of extension twinning systems to prismatic slip systems presently obtained using the binary tree based model, $\frac{250\,\text{MPa}}{5\,\text{MPa}} = 50$, is much larger than any of the values reported in the literature. An important commonality between all these literature values is that they are obtained using the viscoplastic self-consistent model [47]. It will be argued below that the enhanced hardness of extension twinning reflects a change of emphasis from the deformation of the grain bulk in the self-consistent model to the near grain boundary region in the binary tree based model.

In both the viscoplastic self-consistent model [47], and in the present binary tree based model, twinning systems are associated with a single critical resolved shear stress, τ_0, even though it is well-known [3,39,49] that the critical resolved shear stress associated with twin nucleation near grain boundaries is much larger than that associated with twin propagation in the grain bulk. The critical resolved shear stress associated with twinning must, at a minimum, be represented as a step function over the grain domain: a higher value of τ_0 corresponding to twin nucleation near the grain boundaries, and a lower value of τ_0 corresponding to twin propagation in the grain bulk. However, the Chin-Hosford-Mendorf model [31], used here, and also by Tomé et al. [54] makes no such distinction and assumes a single τ_0 for both twinning sub-events. In this context, the physical meaning of τ_0 depends on the sub-granular region of focus of the twinning model, as elaborated below.

The viscoplastic self-consistent model [47], which does not account directly for intergranular interactions across grain boundaries, does not seek to capture the hard slip and twinning modes activated near grain boundaries in order to preserve deformation compatibility (Section II (B.3)). Thus, qualitatively, the grain deformation predicted by the self-consistent model may be regarded as that of the grain bulk, away from the grain boundaries, and the critical resolved shear stress of extension twinning, $\tau_0 = 50$ MPa, must therefore reflect the average resistance to twin propagation through the grain bulk [71].

On the other hand, the binary tree based model allows inhomogeneous grain deformation by sub-dividing grains into ALAMEL regions [53]. It also emphasizes intergranular interactions across grain boundaries through the requirement for deformation compatibility. Strict compatibility with a neighboring ALAMEL region of arbitrary lattice orientation, across an arbitrarily oriented grain boundary facet will not ordinarily be possible by activating only the easy prismatic slip systems. If compatibility constraints demand extension along the $c-$direction, extension twinning systems and/or $<c+a>$ pyramidal slip systems must be activated in the model ALAMEL regions, even if they are considerably harder than prismatic slip. The domain of focus of the binary tree based model is not the grain bulk, but the near grain boundary regions.

The emphasis on near grain boundary behavior in the binary tree based model means that $\tau_0 = 250$ MPa, obtained using the binary tree based model, is the near boundary value of the critical resolved shear stress of extension twinning. Since twinning systems nucleate near grain boundaries [3,39,49], $\tau_0 = 250$ MPa may be regarded as the critical stress for twin nucleation. The present value is larger than the critical stress for twin nucleation in zirconium, 165 MPa, fit by Beyerlein and Tomé [49] using a dislocation ensemble model implemented within the viscoplastic self-consistent framework.

V. CONCLUSIONS

Split channel die plane-strain compression of three zirconium alloy specimens, A1, A2 and B1 with a strong initial texture was performed. A1 and A2 had a similar bimodal grain size distribution, while A1 and B1 has a similar starting texture. The evolution of deformation twinning with strain was mapped. Twinning volume fraction was more sensitive to starting texture than to grain size distribution. Intense near boundary mesoscopic shear strain (NBMS) was observed in all three specimens. NBMS was correlated with deformation twinning.

Polycrystal plasticity simulations based on the binary tree based model for intergranular interaction and the Chin-Hosford-Mendorf [31] model for deformation twinning captured the measured twinning characteristics statistically, provided the hardness of the extension twinning

systems was assumed to be very large. <mark>The emphasis of the binary tree based model on the near grain boundary regions leads to the conclusion that the larger hardness of the twinning systems obtained presently represents the critical stress for twin nucleation.</mark>

ACKNOWLEDGMENTS

REFERENCES

[1]   G.E. Dieter: *Mechanical Metallurgy*, 3rd ed., McGraw-Hill, New York, 1986.

[2]   A. Jain and S.R. Agnew: *Mater. Sci. Eng. A*, 2007, vol. 462, pp. 29–36.

[3]   R.J. McCabe, E.K. Cerreta, A. Misra, G.C. Kaschner, and C.N. Tomé: *Philos. Mag.*, 2006, vol. 86, pp. 3595–3611.

[4]   H. Numakura and M. Koiwa: *Metall. Sci. Technol.*, 1998, vol. 16, pp. 4–19.

[5]   S.G. Song and G.T. Gray: *Metall. Mater. Trans. A*, 1995, vol. 26, pp. 2665–75.

[6]   G.C. Kaschner, C.N. Tomé, I.J. Beyerlein, S.C. Vogel, D.W. Brown, and R.J. McCabe: *Acta Mater.*, 2006, vol. 54, pp. 2887–96.

[7]   K.L. Murty and I. Charit: *Prog. Nucl. Energy*, 2006, vol. 48, pp. 325–59.

[8]   E. Tenckhoff: *J. ASTM Int.*, 2005, vol. 2, pp. 1–26.

[9]   R.J. McCabe, G. Proust, E.K. Cerreta, and A. Misra: *Int. J. Plast.*, 2009, vol. 25, pp. 454–72.

[10]   J.W. Christian and S. Mahajan: *Prog. Mater. Sci.*, 1995, vol. 39, pp. 1–157.

[11]   A.M. Garde, E. Aigeltinger, and R.E. Reed-Hill: *Metall. Trans.*, 1973, vol. 4, pp. 2461–68.

[12]   S.K. Sahoo, V.D. Hiwarkar, I. Samajdar, P. Pant, G.K. Dey, D. Srivastav, R. Tewari, and S. Banerjee: *Mater. Sci. Technol.*, 2010, vol. 26, pp. 104–14.

[13]   J.F. Bingert, T.A. Mason, G.C. Kaschner, P.J. Maudlin, and G.T. Gray III: *Metall. Mater. Trans. A*, 2002, vol. 33A, pp. 955–63.

[14] G.C. Kaschner and G.T. Gray III: *Metall. Mater. Trans. A*, 2000, vol. 31A, pp. 1997–2003.

[15] S. Asgari, E. El-Danaf, S.R. Kalidindi, and R.D. Doherty: *Metall. Mater. Trans. A*, 1997, vol. 28, pp. 1781–95.

[16] E. El-danaf, S.R. Kalidindi, and R.D. Doherty: *Int. J. Plast.*, 2001, vol. 17, pp. 1245–65.

[17] S.R. Kalidindi: *Int. J. Plast.*, 1998, vol. 14, pp. 1265–77.

[18] B. Verlinden, J. Driver, I. Samajdar, and R.D. Doherty: *Thermo-Mechanical Processing of Metallic Materials*, Elsevier (Pergamon Materials Series), 2007.

[19] E. Tenckhoff: *ASTM Spec. Tech. Publ. 966*, 1988, pp. 1–77.

[20] A. Akhtar and A. Teghtsoonian: *Acta Metall.*, 1971, vol. 19, pp. 655–63.

[21] S.K. Sahoo, V.D. Hiwarkar, A. Majumdar, I. Samajdar, P. Pant, G.K. Dey, D. Srivastav, R. Tiwari, and S. Banerjee: *Mater. Sci. Eng. A*, 2009, vol. 518, pp. 47–55.

[22] Y.T. Zhu, X.Z. Liao, X.L. Wu, and J. Narayan: *J. Mater. Sci.*, 2013, vol. 48, pp. 4467–75.

[23] R.J. McCabe, I.J. Beyerlein, J.S. Carpenter, and N.A. Mara: *Nat. Commun.*, 2014, vol. 3806, pp. 1–7.

[24] J. Wang, R.G. Hoagland, J.P. Hirth, L. Capolungo, I.J. Beyerlein, and C.N. Tomé: *Scr. Mater.*, 2009, vol. 61, pp. 903–6.

[25] A. Akhtar: *Metall. Trans. A*, 1975, vol. 6, pp. 1217–22.

[26] T.A. Mason, J.F. Bingert, G.C. Kaschner, S.I. Wright, and R.J. Larsen: *Metall. Mater. Trans. A*, 2002, vol. 33A, pp. 949–54.

[27] P.E. Marshall, G. Proust, J.T. Rogers, and R.J. McCabe: *J. Microsc.*, 2010, vol. 238, pp. 218–29.

[28] R. Kapoor, A. Sarkar, J. Singh, I. Samajdar, and D. Raabe: *Scr. Mater.*, 2014, vol. 74, pp. 72–75.

[29] H. Francillette, B. Bacroix, M. Gasperini, and J.L. Bechade: *Acta Mater.*, 1998, vol. 46, pp. 4131–42.

[30] G. Proust, C.N. Tomé, and G.C. Kaschner: *Acta Mater.*, 2007, vol. 55, pp. 2137–48.

[31] G.Y. Chin, W.F. Hosford, and D.R. Mendorf: *Proc.of R. Soc. London*, 1969, vol. 309, pp. 433–56.

[32] P. Van Houtte: *Acta Metall.*, 1978, vol. 26, pp. 591–604.

[33] C.N. Tomé, R.A. Lebensohn, and U.F. Kocks: *Acta Metall. Mater.*, 1991, vol. 39, pp. 2667–80.

[34] U.F. Kocks, C.N. Tomé, and H.-R. Wenk: *Texture and Anisotropy*, Cambridge University Press, Cambridge, U.K., 1998.

[35] T. Leffers and R.K. Ray: *Prog. Mater. Sci.*, 2009, vol. 54, pp. 351–96.

[36] L. Wang, Y. Yang, P. Eisenlohr, T.R. Bieler, M.A. Crimp, and D.E. Mason: *Metall. Mater. Trans. A*, 2010, vol. 41, pp. 421–30.

[37] L. Wang, P. Eisenlohr, Y. Yang, T.R. Bieler, and M.A. Crimp: *Scr. Mater.*, 2010, vol. 63, pp. 827–30.

[38] T.R. Bieler, L. Wang, A.J. Beaudoin, P. Kenesei, and U. Lienert: *Metall. Mater. Trans. A*, 2014, vol. 45, pp. 109–22.

[39] J. Lind, S.F. Li, R. Pokharel, U. Lienert, A.D. Rollett, and R.M. Suter: *Acta Mater.*, 2014, vol. 76, pp. 213–20.

[40] S. Panchanadeeswaran, R.D. Doherty, and R. Becker: *Acta Mater.*, 1996, vol. 44, pp. 1233–62.

[41] N. Vanderesse, Ch. Desrayaud, S. Girard-Insardi, and M. Darrieulat: *Mater. Sci. Eng. A*, 2008, vol. 476, pp. 322–32.

[42] N. Keskar, S. Mukherjee, K.V. Mani Krishna, D. Srivastava, G.K. Dey, P. Pant, R.D. Doherty, and I. Samajdar: *Acta Mater.*, 2014, vol. 69, pp. 265–74.

[43] H. Paul, J.H. Driver, and W. Wajda: *Mater. Sci. Eng. A*, 2008, vol. 477, pp. 282–94.

[44] I. Samajdar, B. Verlinden, and P. Van Houtte: *ISIJ Int.*, 1998, vol. 38, pp. 759–65.

[45] D. Chapelle and M. Darrieulat: *Mater. Sci. Eng. A*, 2003, vol. 347, pp. 32–41.

[46] G.I. Taylor: *J. Inst. Met.*, 1938, vol. 62, pp. 307–24.

[47] R.A. Lebensohn and C.N. Tomé: *Acta Met. Mater.*, 1993, vol. 41, pp. 2611–24.

[48] S. Mahesh: *Int. J. Plast.*, 2009, vol. 25, pp. 752–67.

[49] I.J. Beyerlein and C.N. Tomé: *Int. J. Plast.*, 2008, vol. 24, pp. 867–95.

[50]   M. Darrieulat, J.-Y. Poussardin, R.-Y. Fillit, and Ch. Desrayaud: *Mater. Sci. Eng. A*, 2007, vol. 445-446, pp. 641–51.

[51]   M.M. Nowell and S.I. Wright: *Ultramicroscopy*, 2005, vol. 103, pp. 41–58.

[52]   T.H. Cormen, C.E. Leiserson, R.L. Rivest, and C. Stein: *Introduction to Algorithms*, Third Edit, MIT press, Cambridge, 2009.

[53]   P.Van Houtte, S. Li, M. Seefeldt, and L. Delannay: *Int. J. Plast.*, 2005, vol. 21, pp. 589–624.

[54]   C.N. Tomé, P.J. Maudlin, R.A. Lebensohn, and G.C. Kaschner: *Acta Mater.*, 2001, vol. 49, pp. 3085–96.

[55]   C. Tomé, G.R. Canova, U.F. Kocks, N. Christodoulou, and J.J. Jonas: *Acta Metall.*, 1984, vol. 32, pp. 1637–53.

[56]   H. Honneff and H. Mecking: in *Proc. 5th Int. Conf. Textures Mater.*, Springer-Verlag, Berlin, 1978, pp. 265–75.

[57]   G.Y. Chin, E.A. Nesbitt, and A.J. Williams: *Acta Metall.*, 1966, vol. 14, pp. 467–76.

[58]   S. Raveendra, A.K. Kanjarla, H. Paranjape, S.K. Mishra, S. Mishra, L. Delannay, I. Samajdar, and P. Houtte: *Metall. Mater. Trans. A*, 2011, vol. 42, pp. 2113–24.

[59]   S.R. Kalidindi, C.A. Bronkhorst, and L Anand: *J. Mech. Phys. Solids*, 1992, vol. 40, pp. 537–69.

[60]   F. Roters, P. Eisenlohr, L. Hantcherli, D.D. Tjahjanto, T.R. Bieler, and D. Raabe: *Acta Mater.*, 2010, vol. 58, pp. 1152–1211.

[61]   A. Zeghadi, S. Forest, A.-F. Gourgues, and O. Bouaziz: *Philos. Mag.*, 2007, vol. 87, pp. 1425–46.

[62]   W.J. McG. Tegart: *Philos. Mag.*, 1964, vol. 9, pp. 339–41.

[63]   P.G. Partridge: *Met. Rev.*, 1967, vol. 12, pp. 169–94.

[64]   M.L. Picklesimer: *J. Electrochem. Soc.*, 1966, vol. 4, pp. 289–300.

[65]   J.L. Martin and R.E. Reed-Hill: *Trans. Met. Soc. AIME*, 1964, vol. 230, pp. 780–85.

[66]   E.J. Rapperport: *Acta Metall.*, 1959, vol. 7, pp. 254–60.

[67]   R.A. Lebensohn, M.I. Gonzalez, C.N. Tomé, and A.A. Pochettino: *J. Nucl. Mater.*, 1996, vol. 229, pp. 57–64.

[68] E. Girard, R. Guillen, P. Weisbecker, and M. Francois: *J. Nucl. Mater.*, 2001, vol. 294, pp. 330–38.

[69] D. Gloaguen, T. Berchi, E. Girard, and R. Guillén: *Acta Mater.*, 2007, vol. 55, pp. 4369–79.

[70] L. Capolungo, I.J. Beyerlein, G.C. Kaschner, and C.N. Tomé: *Mater. Sci. Eng. A*, 2009, vol. 513-514, pp. 42–51.

[71] M. Barnett, M. Setty, and F. Siska: *Metall. Mater. Trans. A*, 2013, vol. 44, pp. 2962–69.
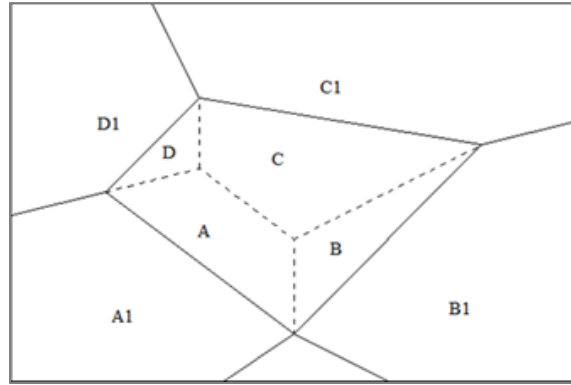
(a)
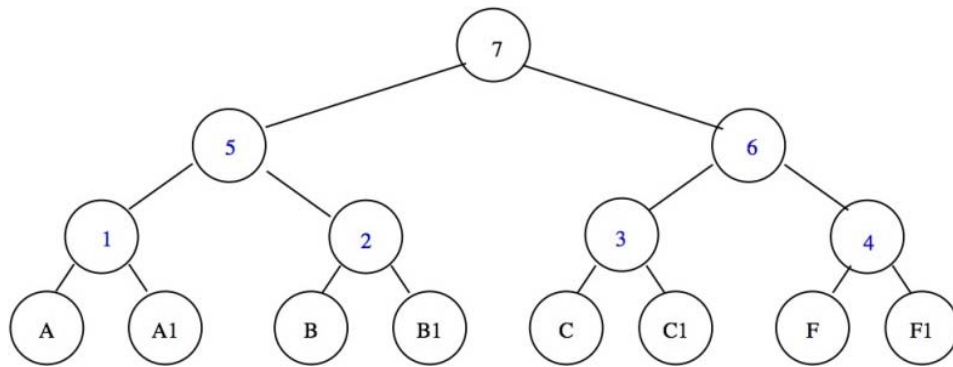
(b)

Figure 1: Binary tree based model [48] of a schematic idealized microstructure. (a) Idealized microstructure; (b) Balanced binary tree representation of (a).

Punch

Split Samples

Die

TD
RD
ND

Z

Y

X

ND
TD
RD
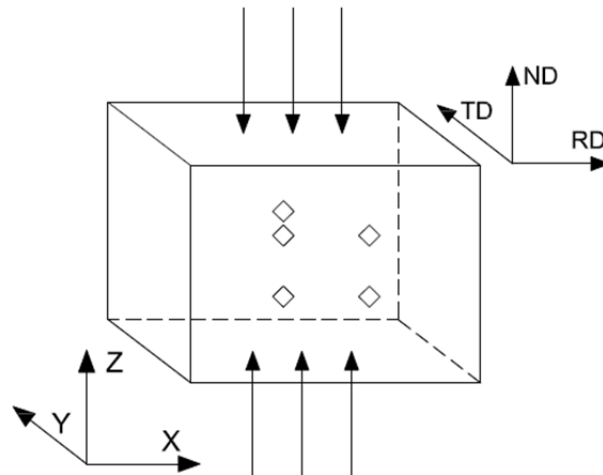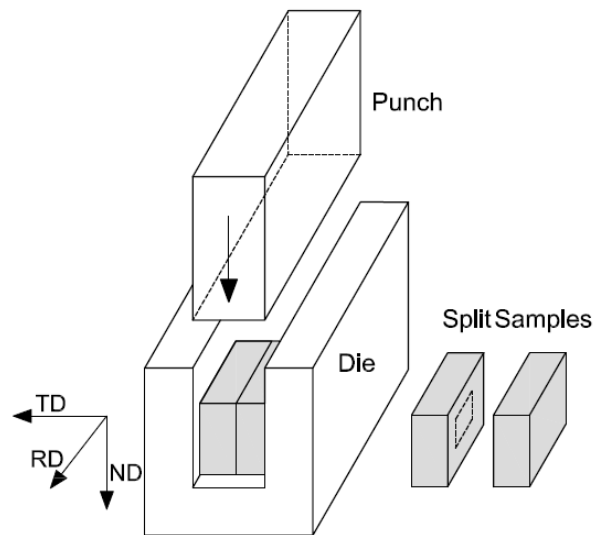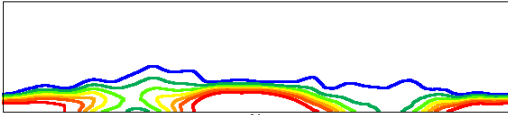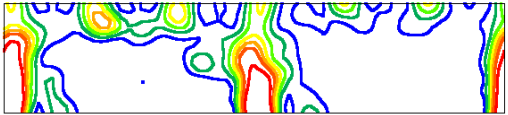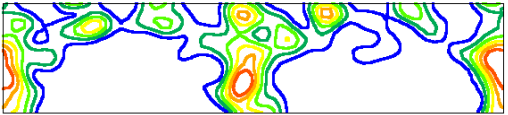
A = Hot Extruded
B = Hot Extruded + Annealed

X = Extrusion (Axial) Direction
Y & Z = Radial Directions
(with respect to extrusion
co-ordinate system)

RD, TD, ND = Rolling, Transverse
and Normal Directions
(with respect to split channel die)

A1: RD = Z, TD = Y, ND = X
A2: RD = X, TD = Y, ND = Z
B1: RD = X, TD = Y, ND = Z

(a)

	Sample A1	Sample A2	Sample B1
ODF 8.000 6.000 5.000 4.000 3.000 2.000 1.000	$f(g)_{max}$ = 19.06 TI = 4.93	$f(g)_{max}$ = 15.9 TI = 3.63	$f(g)_{max}$ = 8.77 TI = 2.94

(b)
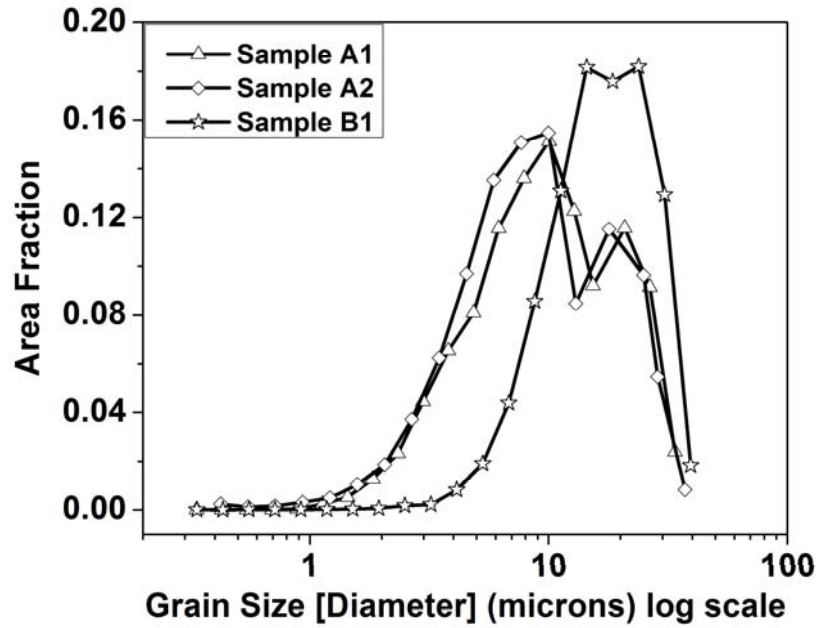
(c)
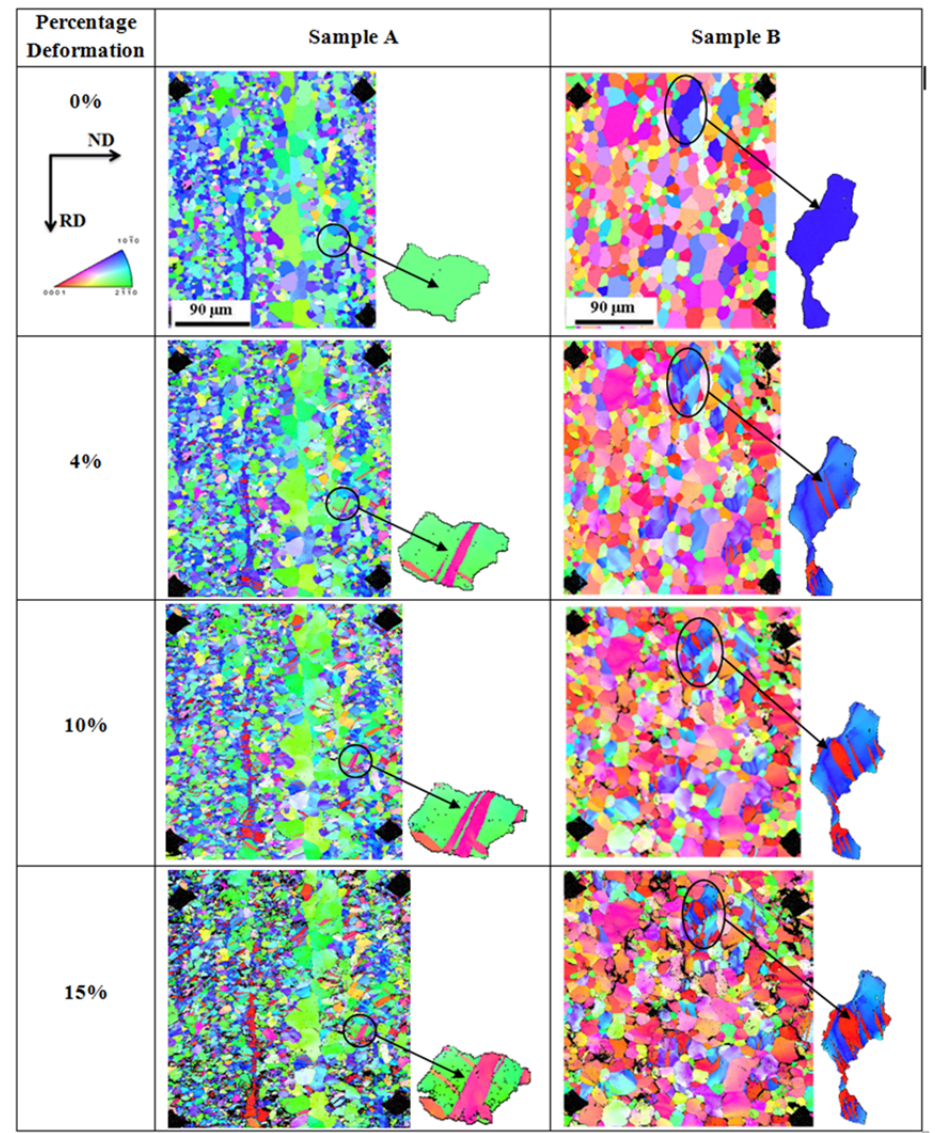
(d)

Figure 2: (a) Schematic drawing of the split channel die plane strain compression (SCDPSC) set-up. Three different samples were used: A1, A2 and B1. (b) Starting texture of all the specimens at the $\varphi_2 = 30°$ ODF section. Both maximum ODF intensities ($f(g)_{max}$) and texture indices (TI: Eq. (21)) are indicated. (c) Grain size distribution of the respective samples. (d) EBSD (electron backscattered diffraction) IPF (inverse pole figure) maps of samples A1 and B1 after different SCDPSC reductions. Insets show formation of deformation twins in representative grains of both samples.
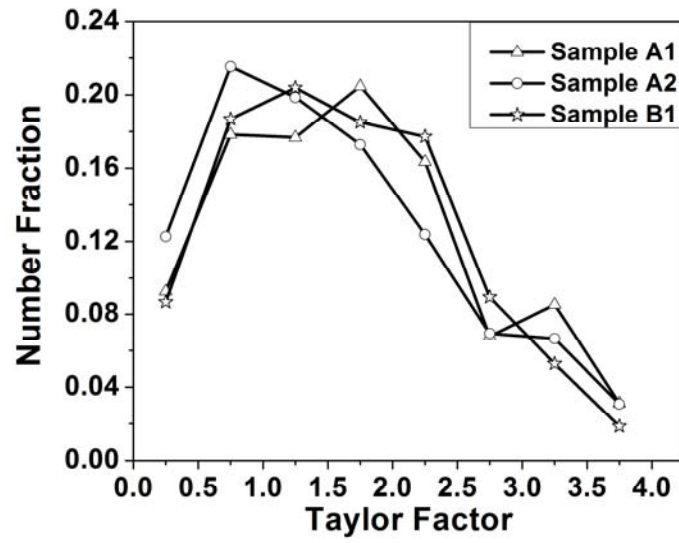
(a)
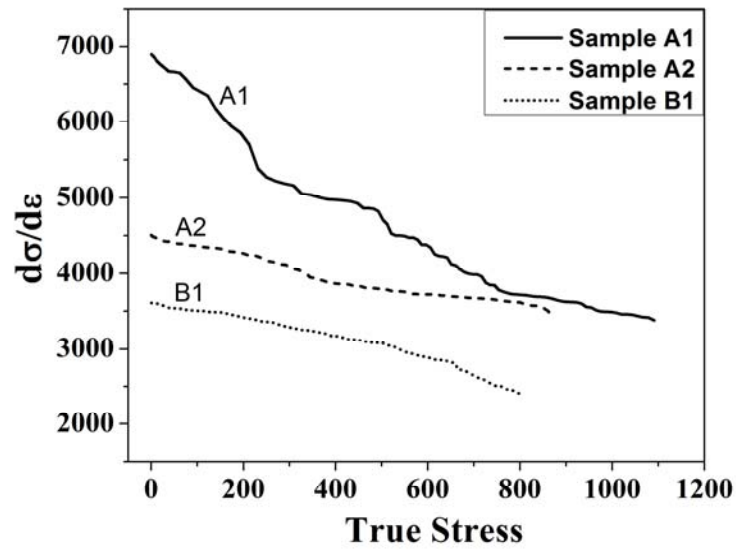
(b)

Figure 3: (a) Taylor factor distributions and (b) work-hardening behavior of specimens A1, A2 and B1.
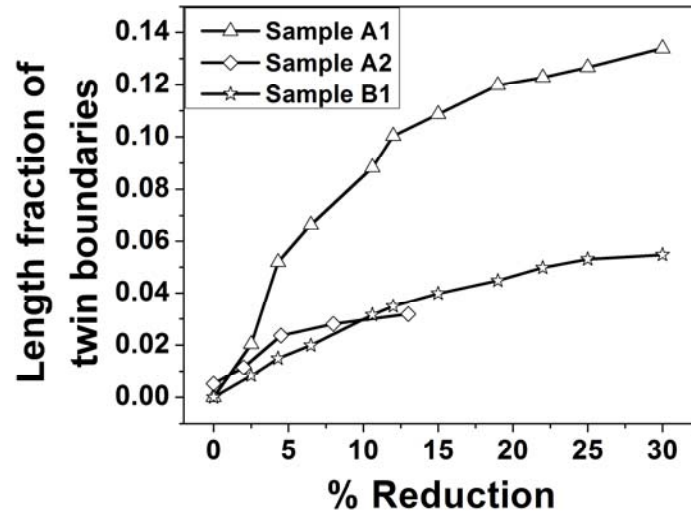
(a)
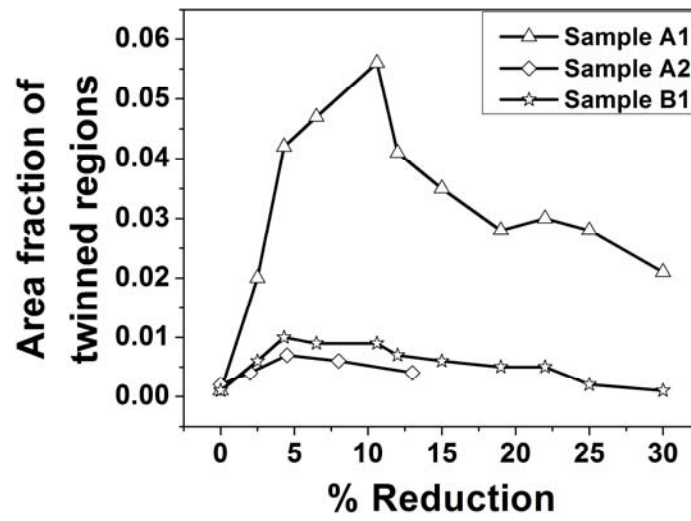
(b)

Figure 4: (a) Length fraction of twin boundaries and (b) area fractions of twinned regions versus percentage reduction. Results were obtained by manual separation of such boundaries and regions.
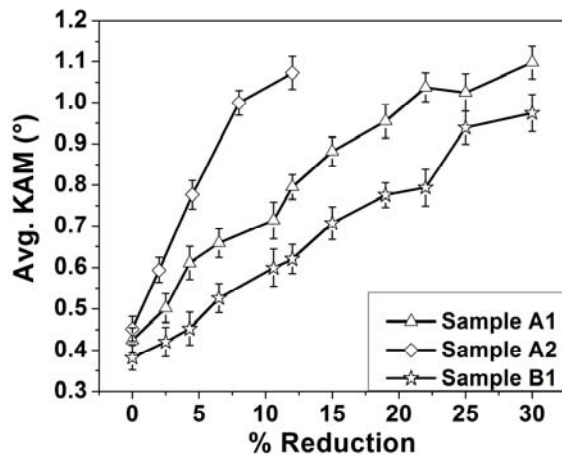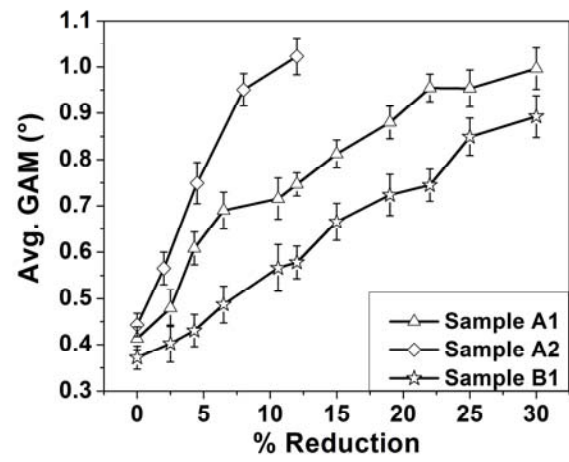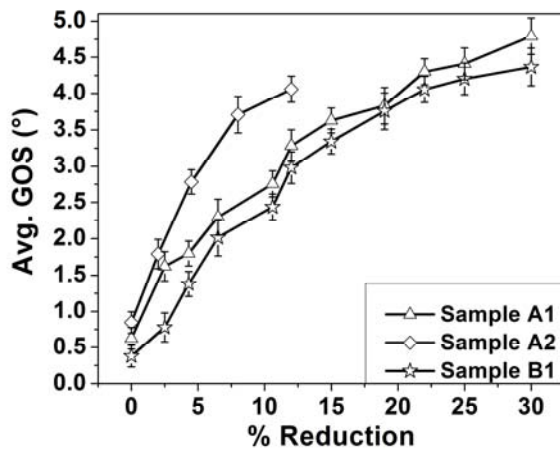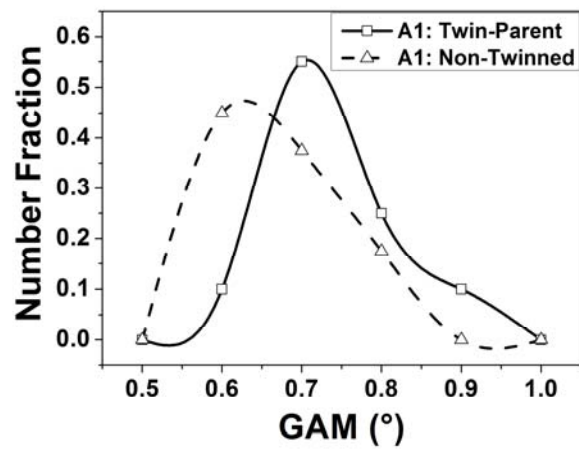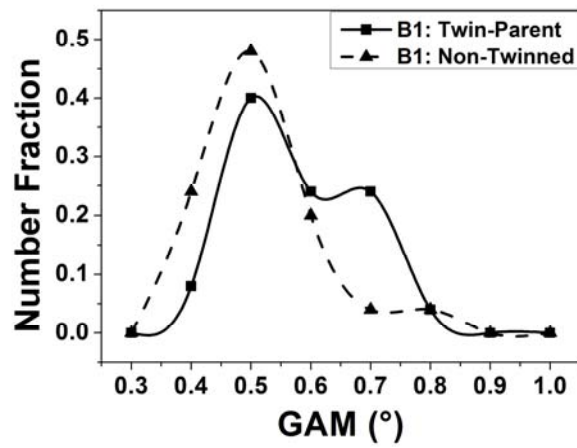
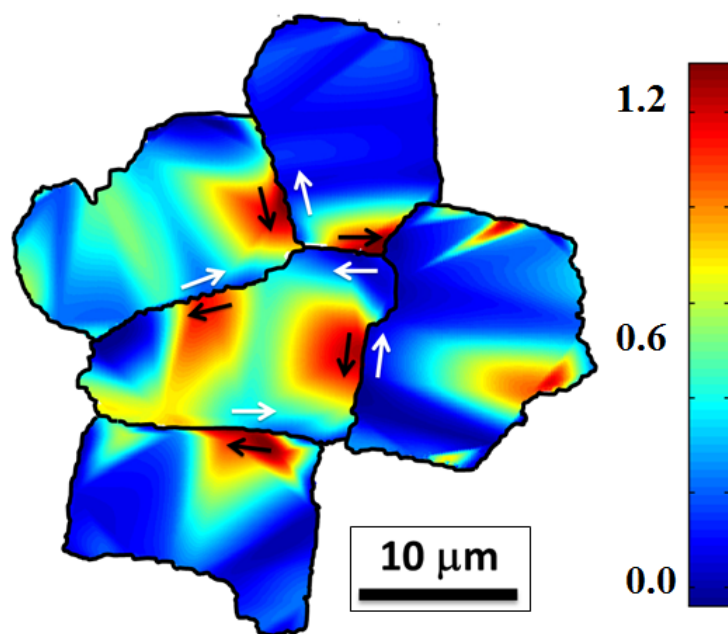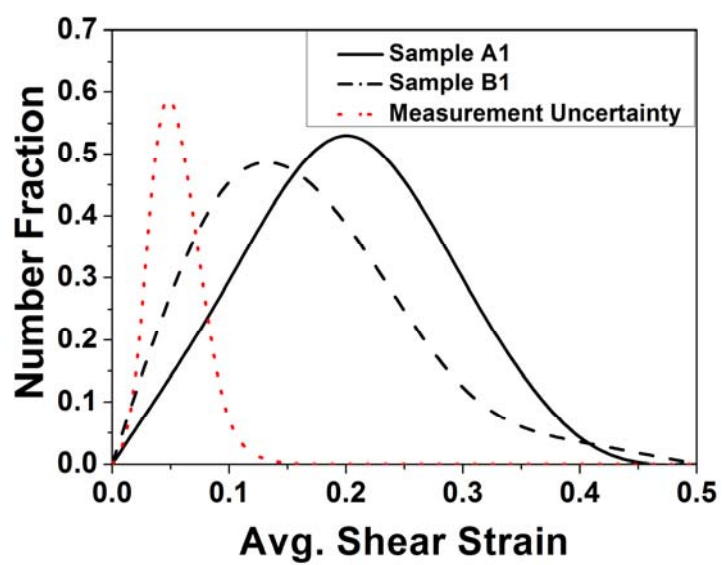**Figure 5:** Development of average (a) KAM, (b) GAM and (c) GOS with percentage reduction. Error bars indicate standard deviations in EBSD data. GAM distributions between twin-parent and non-twinned grains in samples (d) A1 and (e) B1.
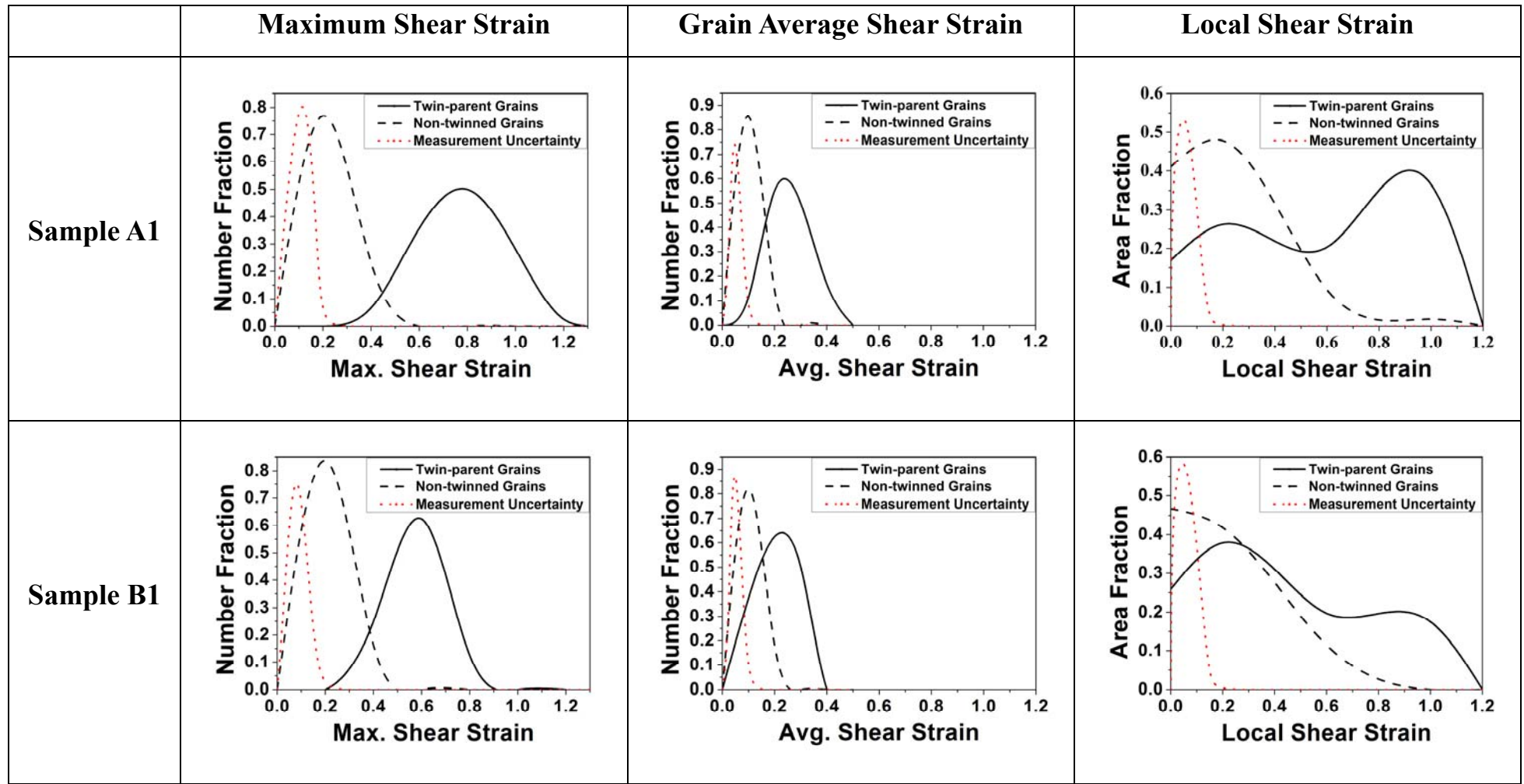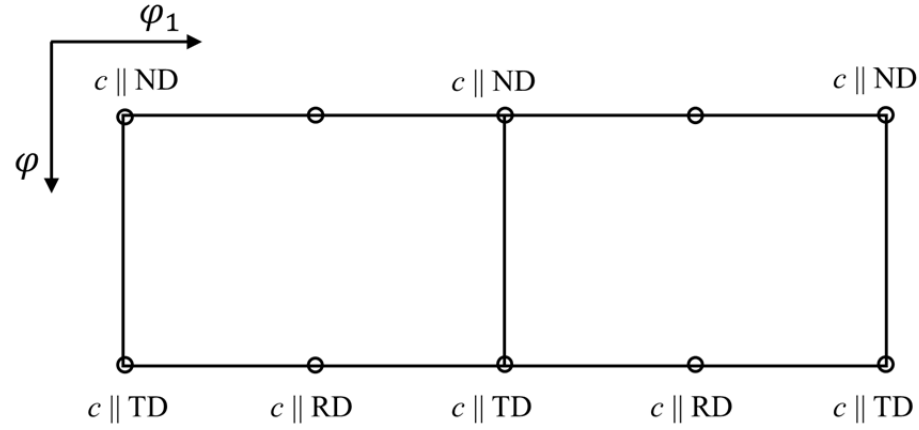
(a)

(b)

(c)

Figure 6: Near boundary mesoscopic shear (NBMS) strains were measured [42] from EBSD maps. (a) An example of NBMS from a grain cluster after about 4% reduction by SCDPSC in sample A1. Arrowheads are used to show positive and negative shear directions. Comparisons between specimens A1 and B1 as: (b) average NBMS and (c) maximum, average and local NBMS. (c) is shown for twin-parent and non-twinned grains. (b) and (c) are plotted at ~10% reduction by SCDPSC.
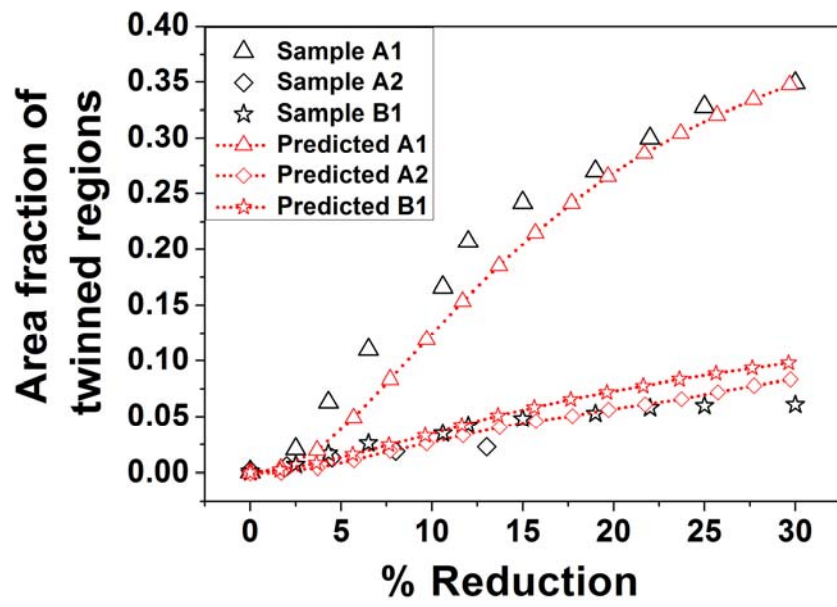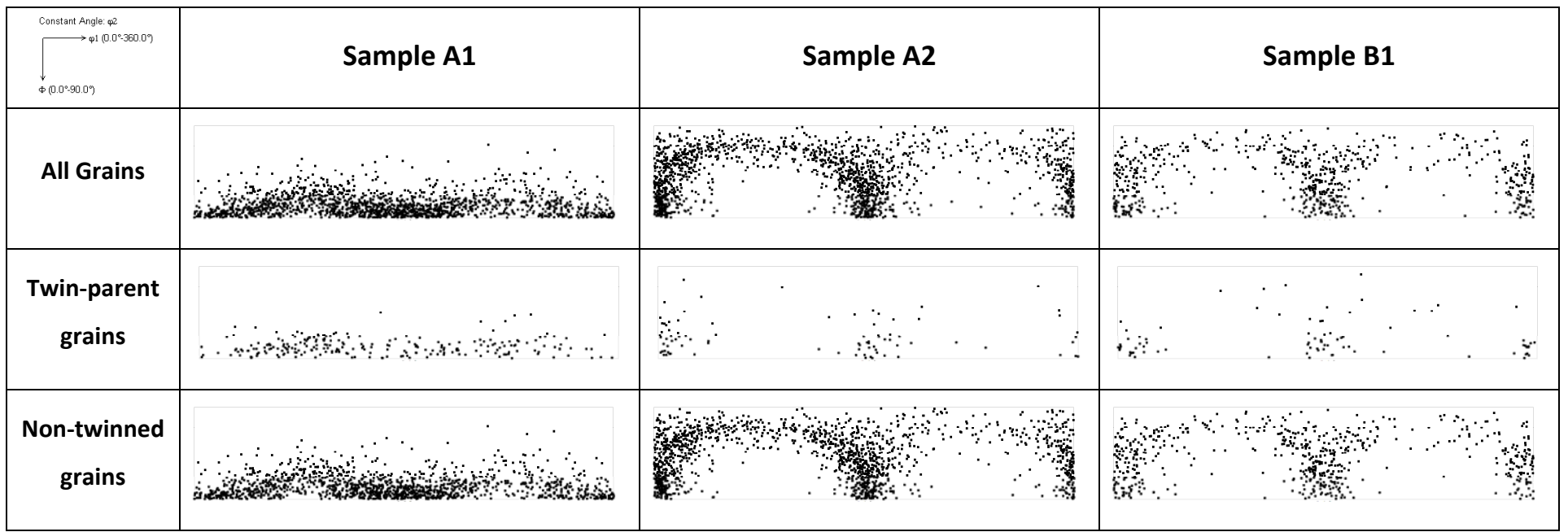
Figure 7: Predicted and experimental evolution of the area fraction of twinned regions with percentage reduction in specimens A1, A2 and B1.
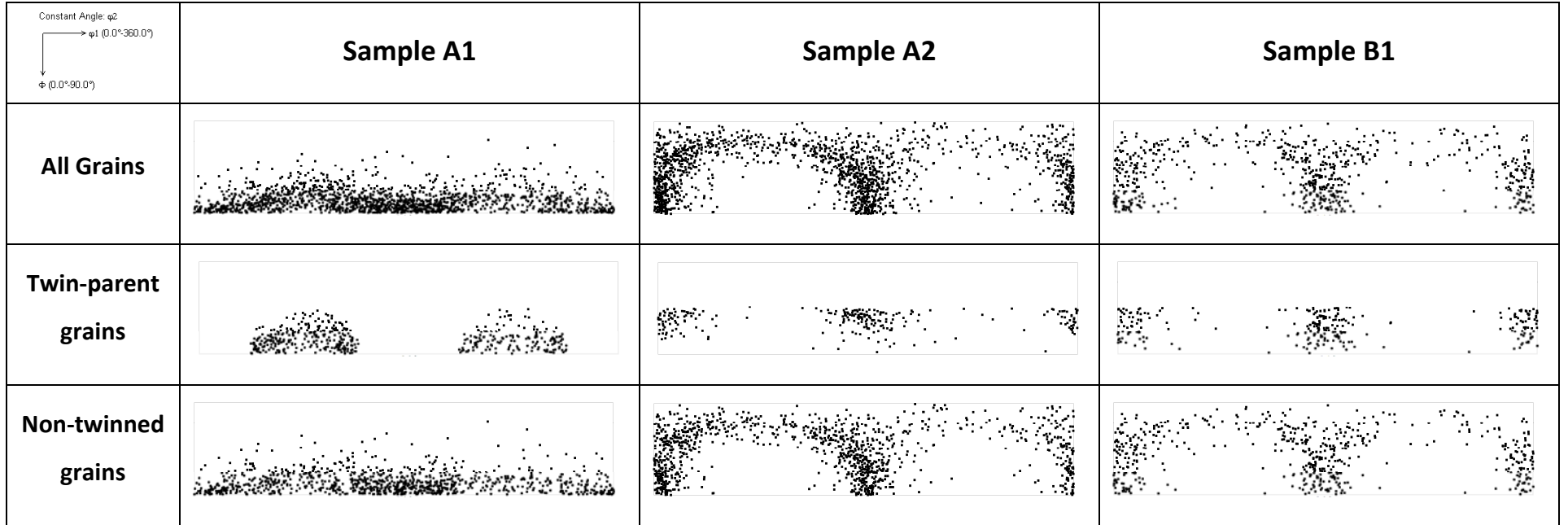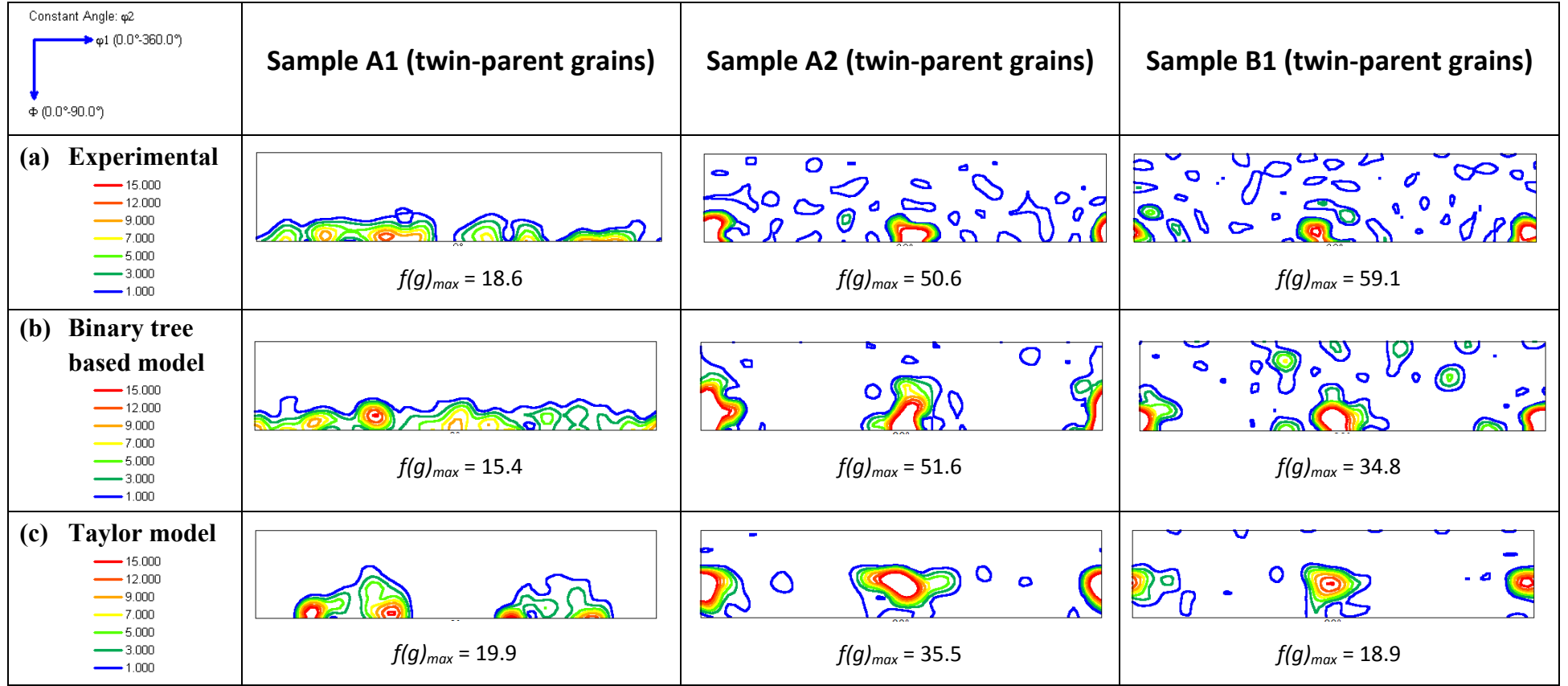
(a)

(b)

Figure 8: (a) Location of special orientations in the $\varphi_1 - \varphi$ Euler space map. (b) Euler space representation of all physical grains, twin-parent grains and non-twinned grains after $\varepsilon = 0.04$ (~4% SCDPSC). (c) Binary tree based model predictions. (d) Relaxed constraint (RC) Taylor model predictions.

Constant Angle: φ2 φ1 (0.0°-360.0°) Φ (0.0°-90.0°)	Sample A1 (twin-parent grains)	Sample A2 (twin-parent grains)	Sample B1 (twin-parent grains)
(a) **Experimental** — 15.000 — 12.000 — 9.000 — 7.000 — 5.000 — 3.000 — 1.000	$f(g)_{max}$ = 18.6	$f(g)_{max}$ = 50.6	$f(g)_{max}$ = 59.1
(b) **Binary tree based model** — 15.000 — 12.000 — 9.000 — 7.000 — 5.000 — 3.000 — 1.000	$f(g)_{max}$ = 15.4	$f(g)_{max}$ = 51.6	$f(g)_{max}$ = 34.8
(c) **Taylor model** — 15.000 — 12.000 — 9.000 — 7.000 — 5.000 — 3.000 — 1.000	$f(g)_{max}$ = 19.9	$f(g)_{max}$ = 35.5	$f(g)_{max}$ = 18.9

Figure 9: φ_2 =30° ODF sections of the twin-parent grains after ε = 0.04 (~4% SCDPSC). (a) Experimental, (b) Binary tree based model predictions and (c) Taylor model predictions.
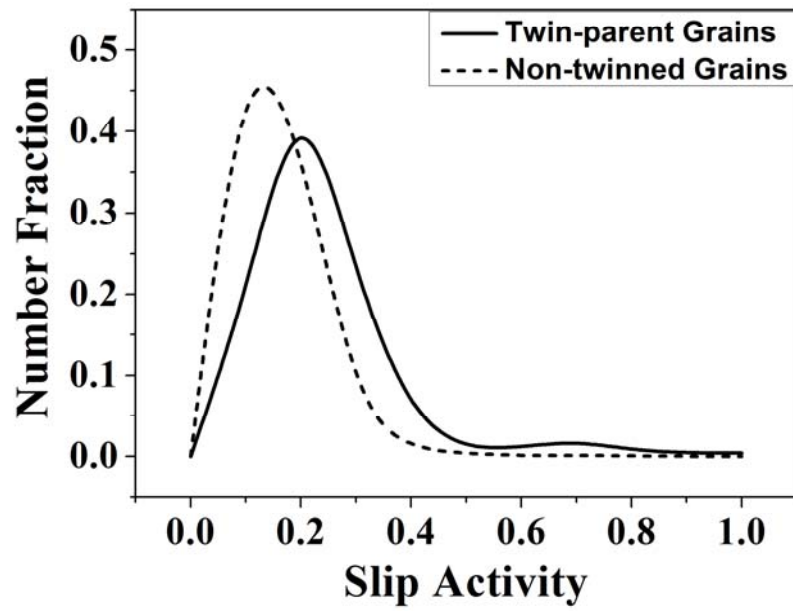
Figure 10: Slip activity in predicted in Sample A1 for twin-parent grains and non-twinned grains at 4% reduction.

Table I: Chemical composition of the Zircaloy-4 used in this study.

Elements	Sn (wt. %)	Fe (wt.%)	Cr (wt.%)	Al (ppm)	Hf (ppm)	C (ppm)	Zr
	1.5	0.22	0.1	39.0	<50	<55	Balance

Table II: Parameters describing the evolution of threshold stress with deformation for the deformation modes at room temperature.

System(s)	τ_0 (MPa)	τ_1 (MPa)	θ_0 (MPa)	θ_1 (MPa)	Self-hard h^{ss}	Latent hardening $h^{s\ pr}$	$h^{s\ pyr}$	$h^{s\ ttw}$
Prismatic $\{10\bar{1}0\} < \bar{1}2\bar{1}0 >$	5	30	1500	50	1	1	1	10
Pyramidal $\{10\bar{1}1\} < \bar{1}\bar{1}23 >$	70	270	3000	25	1	1	1	10
Extension twinning $\{10\bar{1}2\} < \bar{1}011 >$	250	0	75	75	1	1	1	10